

SPACE TELESCOPE IMAGING SPECTROGRAPH CORONAGRAPHIC OBSERVATIONS OF β PICTORIS¹

SARA R. HEAP, DON J. LINDLER,² THIERRY M. LANZ,³ ROBERT H. CORNETT,⁴ AND IVAN HUBENY⁵

Laboratory for Astronomy and Solar Physics, Code 681, NASA Goddard Space Flight Center, Greenbelt, MD 20771; heap@stis.gsfc.nasa.gov, lindler@stis.gsfc.nasa.gov, lanz@stis.gsfc.nasa.gov, cornett@stis.gsfc.nasa.gov, hubeny@stis.gsfc.nasa.gov

S. P. MARAN

Space Sciences Directorate, Code 600, NASA Goddard Space Flight Center, Greenbelt, MD 20771; maran@stis.gsfc.nasa.gov

AND

BRUCE WOODGATE

Laboratory for Astronomy and Solar Physics, Code 681, NASA Goddard Space Flight Center, Greenbelt, MD 20771; woodgate@stis.gsfc.nasa.gov

Received 1997 December 18; accepted 2000 February 23

ABSTRACT

We present new coronagraphic images of β Pictoris obtained with the Space Telescope Imaging Spectrograph (STIS) in 1997 September. The high-resolution images ($0''.1$) clearly detect the circumstellar disk as close to the star as $0''.75$, corresponding to a projected radius of 15 AU. The images define the warp in the disk with greater precision and at closer radii to β Pic than do previous observations. They show that the warp can be modeled by the projection of two components: the main disk and a fainter component, which is inclined to the main component by 4° – 5° and extends only as far as $\approx 4''$ from the star. We interpret the main component as arising primarily in the outer disk and the tilted component as defining the inner region of the disk. The observed properties of the warped inner disk are inconsistent with a driving force from stellar radiation. However, warping induced by the gravitational potential of one or more planets is consistent with the data. Using models of planet-warped disks constructed by Larwood & Papaloizou, we derive possible masses of the perturbing object.

Subject headings: accretion, accretion disks — circumstellar matter — planetary systems — stars: imaging — stars: individual (β Pictoris)

1. INTRODUCTION

The extensive circumstellar disk of β Pic has been subjected to intense scrutiny and interpretation since it was discovered by Smith & Terrile (1984). These studies have been inspired by the possibility that the β Pic system might be an analogue to the solar system in its early stages or represent a distinct branch of planetary system evolution. In either case, β Pic provides a laboratory in which cosmological theories can be tested. Nevertheless, 15 years after its discovery, the β Pic circumstellar system remains largely a mystery. Is β Pic a protoplanetary environment, in which planets have not yet formed, one where planets already exist, or a “failed” system, where planetesimals, if any, cannot grow further? Spectroscopic indications of cometary bodies (e.g., Vidal-Madjar et al. 1994) suggest that planet-building has progressed at least to the planetesimal stage but resolve few issues. These questions are thoroughly reviewed by Artymowicz (1997) from pre-1997 data. Although there is no direct evidence for planets around β Pic, there are intriguing asymmetries in the disk that may be due to gravitational perturbations by substellar objects. The most important of these is a reported 3° tilt of the inner disk ($r < 50$ AU) with respect to the outer disk (Burrows et al. 1995; Mouillet et al. 1997).

We present new coronagraphic observations made with the Space Telescope Imaging Spectrograph (STIS), as installed on the *Hubble Space Telescope (HST)* in 1997 February. The STIS coronagraphs show a greater level of detail, provide higher image quality, and reveal the disk closer to the star than prior observations. These observations further characterize the tilt of the inner disk for comparison with theory. In § 2, we describe the design and performance of the STIS coronagraph. In § 3, we discuss the β Pic observations and data reduction techniques. In § 4, we present the observational results. The STIS images show the disk to be warped at close radii to the star in the sense that the inner disk is tilted by 4.6° with respect to the outer disk. In § 5, we use the size and shape of the warp to evaluate the two proposed theories of its origin. We conclude that the observations of the warp in the inner disk favor the existence of a planet around β Pic.

2. STIS CORONAGRAPHY

Although designed primarily for spectroscopy, STIS easily meets the prime requirements for stellar coronagraphy. It employs an occulting mask and Lyot stop that work together to block out direct and scattered starlight. Because of its high resolution, $0''.1 = 2$ AU at the *Hipparcos* distance of β Pic (19.28 pc), it can accommodate small occulting masks, thereby allowing examination of the β Pic disk to within $0''.5$, or a projected distance of 10 AU, from the star. Most importantly, its stable point-spread function makes possible a definitive separation of the disk’s light from other components. In contrast, Wide Field and Planetary Camera 2 (WFPC2) lacks a coronagraphic mode; and ground-based coronagraphs, even with adaptive optics, are subject to significant variations in the point-spread function

¹ Based on observations with the NASA/ESA *Hubble Space Telescope*, obtained at the Space Telescope Science Institute, which is operated by the Association of Universities for Research in Astronomy, Inc., under NASA contract NAS5-26555.

² Advanced Computer Concepts, Potomac, MD 20854.

³ Department of Astronomy, University of Maryland, College Park, MD 20742.

⁴ Raytheon Information Technology and Scientific Services, 4400 Forbes Boulevard, Lanham, MD 20706.

⁵ National Optical Astronomy Observatories, Tucson, AZ 85726.

(PSF). Below, we describe the design and performance of the STIS coronagraph.

The STIS design is described by Woodgate et al. (1998), its in-orbit performance, by Kimble et al. (1998), and its in-orbit operations, by Sahu et al. (1999) in the STIS Handbook. Figure 1 shows the optical layout of the STIS coronagraph. Light entering the instrument is corrected for telescope aberrations and for astigmatism at the STIS field point by a two-mirror system similar to that used in Corrective Optics Space Telescope Axial Replacement (COSTAR). After correction, light passes through the coronagraphic aperture mask at the first STIS focal plane. The beam is collimated by an off-axis ellipsoidal mirror and directed to a flat mirror near the second pupil plane, a few millimeters beyond the Lyot stop. The beam then goes to a folding flat and an ellipsoidal camera that focuses the light onto the CCD detector.

Coronagraphic observations on STIS make use of an occulting mask, called 50CORON in the STIS Handbook, which is one of 65 apertures that can be inserted into the beam at the focal plane. Its format is clearly seen in Figure 2, which shows a coronagraphic image of HD 60753, a $V = 6.61$ B3 III-type star having no known circumstellar structure. The square field is $51''$ across. The 50CORON aperture mask has a large rectangular bar $3'' \times 10''$ (*top of figure*) and two tapered bars (*wedges*) ranging in width from $0''.5$ to $3''$. For these observations, the star was positioned behind WedgeB1.8, a point at which the bar is $1''.8$ wide.

The halo of the *HST* PSF is caused largely by light with phase errors from the sagged outer radii of the primary mirror, with some contribution from light diffracted from the edges of the *HST* primary (Vaughn 1991). A conventional Lyot stop is a baffle at a pupil plane shaped to block light from these sources. The STIS Lyot stop, which is near

but not precisely at a pupil plane, is a circular aperture open to the central 77% of the beam area. It is expected to eliminate error light from both mirror sag and the primary edge. A comparison of theoretical and observational data on β Pic suggests that the Lyot stop decreases the intensity of the PSF halo by a factor of 2, but further observations will be needed to quantify the effectiveness of the Lyot stop.

The detector is a back-thinned, UV-enhanced CCD with a 1024×1024 pixel format, each pixel subtending $0''.0507$. Hence, one CCD pixel subtends nearly exactly 1 AU at the distance of β Pic. The intrascene dynamic range of the CCD in a single exposure is 20,600; it can be effectively increased by combining a series of exposures to raise the count statistics while beating down the read noise. The low readout noise ($1.7 \text{ DN} = 6.8 e^-$) and dark current ($6 e^- \text{ pixel}^{-1} \text{ hr}^{-1}$) make it possible to probe the β Pic disk out to very low surface brightness.

Since the 50CORON aperture is unfiltered, the UV-enhanced CCD records light over a very wide band, from 2000 to 10000 Å. The effective PSF is therefore an average of monochromatic PSFs, each weighted by the stellar flux recorded by the CCD at the corresponding wavelength. The broad response of the detector has the important advantage of blending the diffraction rings, thereby erasing color-dependent structure in the PSF and producing a smooth halo. However, the sensitivity at long wavelengths increases the influence of scattering within the detector. At longer wavelengths, the wings of the PSF are visible out to several hundred pixels from the stellar spectrum.

The coronagraphic image shown in Figure 2 was obtained during the test and evaluation of STIS following its installation on *HST* in 1997 February. Unfortunately, the innermost regions of the PSF are saturated ($> 144,000 e^-$). Nevertheless, the deep exposure is useful in revealing

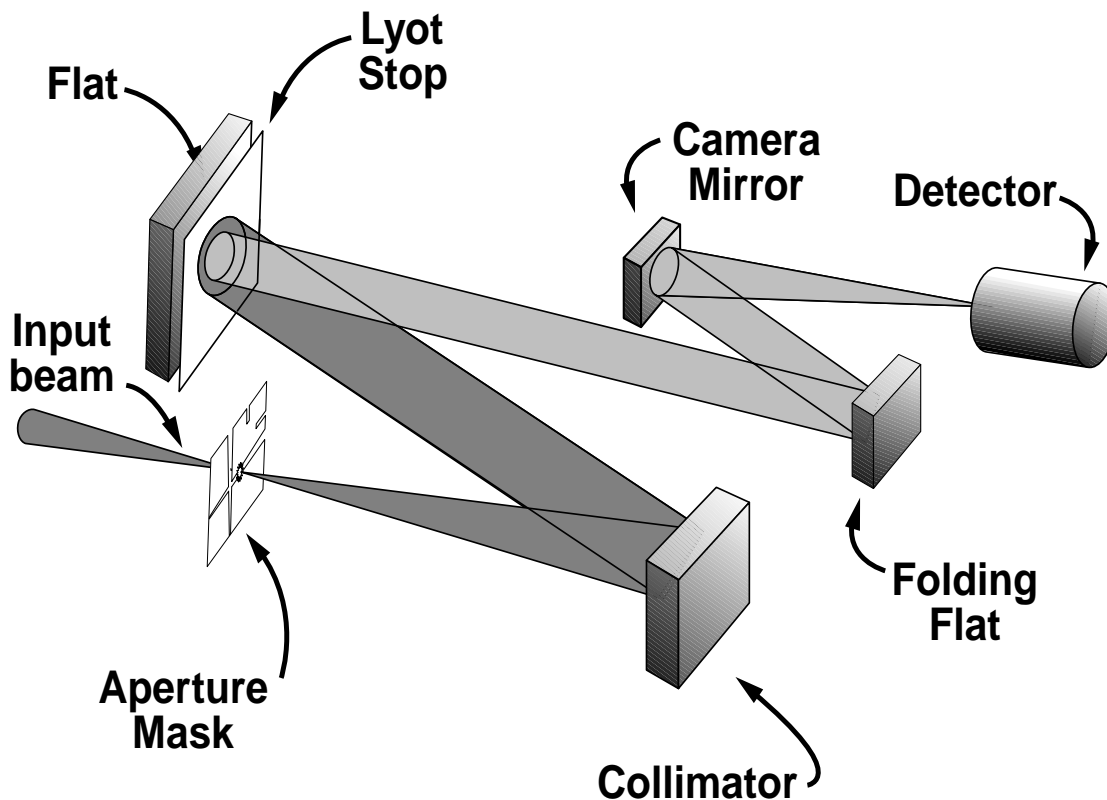


FIG. 1.—Optical layout of the STIS coronagraph

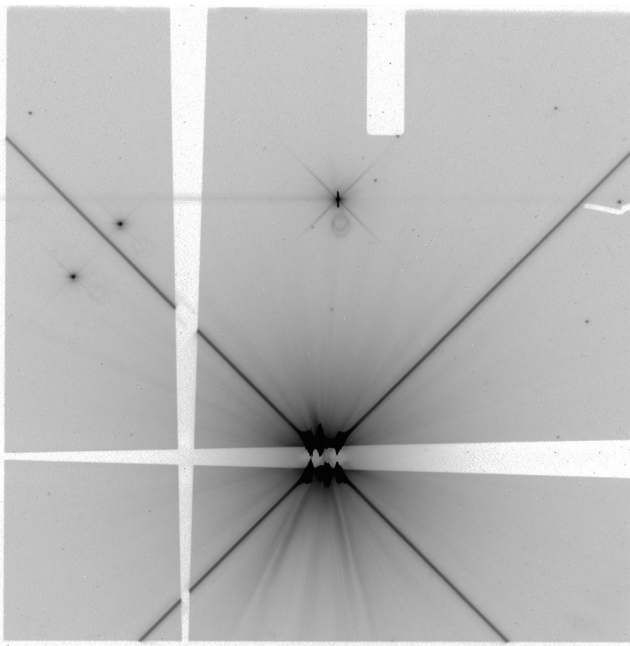


FIG. 2.—Format of a STIS coronagraphic image as shown by an observation of HD 60753 ($V = 6.61$, $B - V = -0.09$, spectral type = B3 III), a single star having no known circumstellar structure. The field is $51''$ across. The data were obtained as part of Servicing Mission Orbital Verification (SMOV) program 7088 to test the coronagraphic mode of STIS. The image shown here is a raw image displayed on a logarithmic scale. It is one of three exposures comprising the WedgeB1.8 observation of the star.

structure of the PSF far from the star. The residual starlight outside the occulting bar has unexpected structure. The main features are the small “tuft of hair” that juts out to the upper left from the occulted region and the two long “stool legs” that project downward from the position of the occulted star. The origins of these artifacts are unknown, but they are permanent features of the PSF. Because of this general stability, the PSF can be removed or greatly suppressed from the observations.

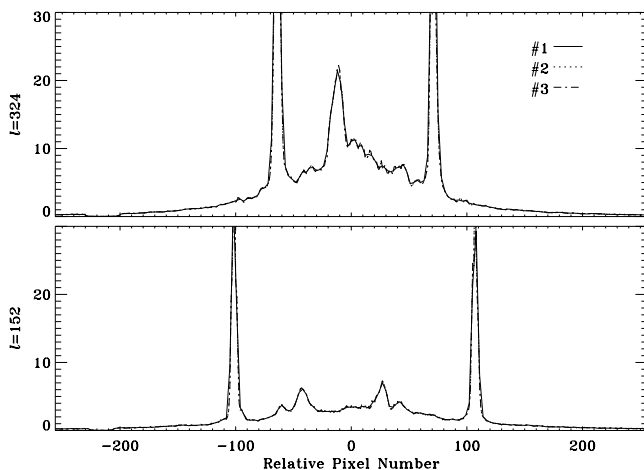


FIG. 3.—Stability of the PSF during the observation of HD 60753. Each exposure is identified by a line type as given in the legend. The cross-sectional profiles are taken at line positions, $l = 324$ (top) through the “tuft of hair” and $l = 152$ (bottom) through the “stool legs.” The stability of the PSF is such that the three exposures cannot be distinguished from one another. The two bright spikes in either plot are the telescope diffraction spikes.

In principle, the PSF could be degraded by telescope guidance errors and jitter and by thermal drifts within STIS. In practice, such errors are so small that they can be ignored. However, the telescope is known to experience focus variations (“breathing”) that take place on a time-scale of only minutes. Comparison of the three 10 minute exposures that comprise the observation of HD 60753 indicates that the effects of such variations are insignificant compared with the intrinsic structure in the PSF. As a demonstration, Figure 3 shows cross-sectional plots of the three exposures. Only in the diffraction spikes can one exposure be distinguished from another. We have found similar stability in our series of exposures of β Pic. Evidently, telescope “breathing” does not noticeably affect the PSF at distances of $1''$ or more from the star if the exposures are all taken in the same orbit.

3. OBSERVATIONS AND REDUCTION

3.1. Observing Strategy and Procedure

Typically, the observing procedure for coronagraphy involves identical observations of the target and a nearby reference star of similar magnitude and spectral type. The intensity-scaled image of the reference star is then subtracted from the target image in order to remove starlight in the target image that was not already blocked by the occulting mask and Lyot stop. This procedure was not followed in our observations of β Pic. Instead, we observed only the β Pic system, but at three different spacecraft roll angles: a roll angle that orients the β Pic disk midway between the telescope diffraction spikes, and at roll angles -12° and $+14^\circ$ from the first.

This observing strategy offers two important benefits. The first is reliable detection of structure in the β Pic disk, if present. If an apparent structure remains fixed in images taken at different roll angles, then the feature must be due to the PSF or some detector blemish such as a “hot” pixel; but if the apparent structure rotates with the telescope, then it is identified as originating in the disk. The method of roll separation may not work close to the star if the thickness of the disk is comparable to the linear distance moved between roll angles. In that case, any azimuthally symmetric component of the disk would be rejected and falsely attributed to the PSF. The method of roll separation should be checked by direct subtraction of the PSF as defined by a suitable reference star.

The second advantage of roll separation is suppression of noise induced by the inevitably imperfect determination of the flat-field correction. In the reduction, we flat-fielded the β Pic images using an imaging flat of a tungsten lamp. Since β Pic and the tungsten lamp have different spectral flux distributions, the standard flat will have residual errors when applied to β Pic. These residuals are averaged out by observing the disk at different orientations.

Another planning issue is the choice of occulting bar width to be used. The ideal occulting bar is small enough to allow a probe of the β Pic disk close in to the star but large enough that light from the star does not overwhelm the light from the disk or saturate the detector. We chose to make observations at two spots along the occulting bar: at WedgeB1, which allows a probe to within $r = 0.5'' = 10$ AU from the star, and at WedgeB2, to within $r = 1'' = 20$ AU.

The observations were taken on 1997 September 16–17 as part of the program of *HST* early-release observations

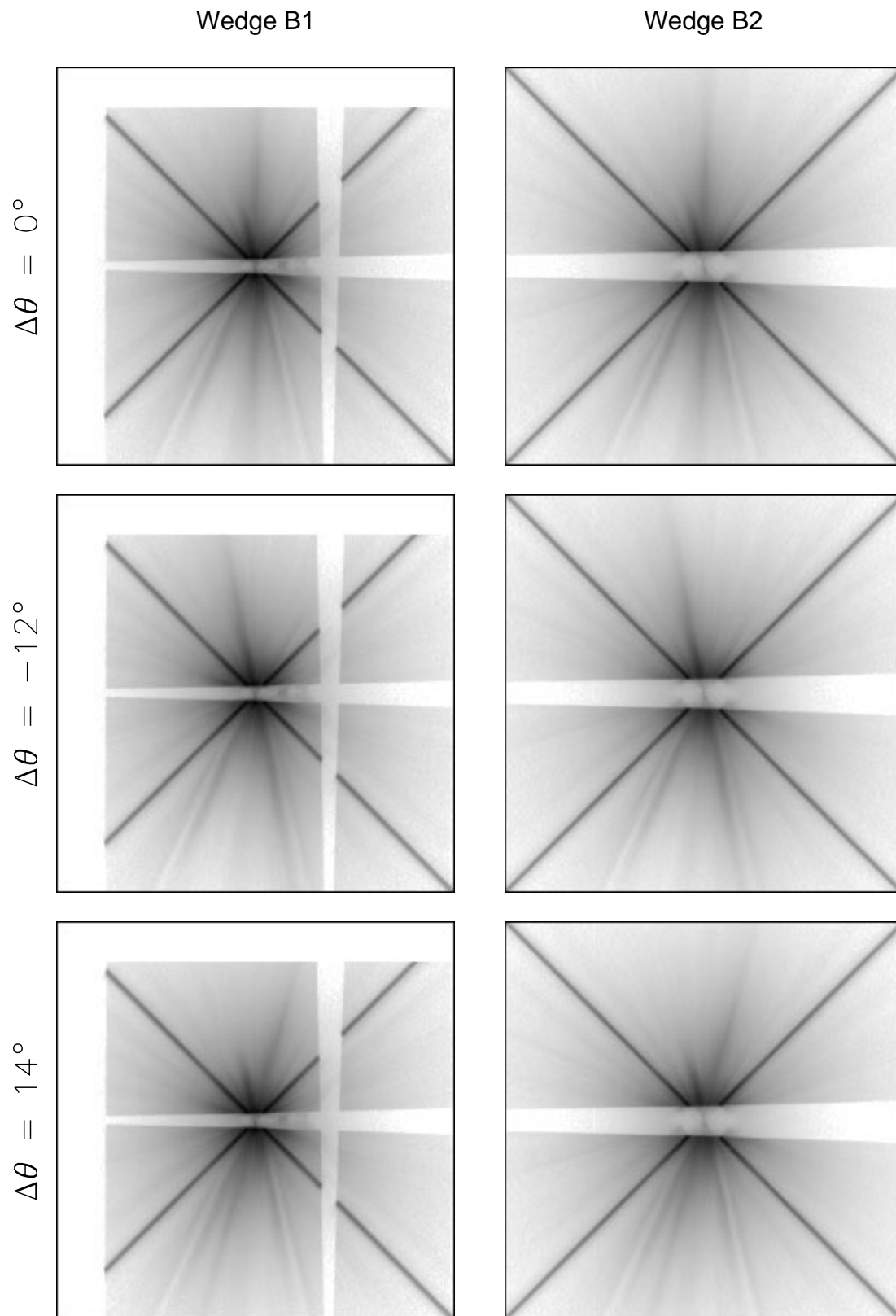


FIG. 4.—Solutions for the β Pic disk based on WedgeB1 data. The software masks are not applied in these displays, in order to show the location of the disk relative to the occulting wedges and telescope diffraction spikes. Each square box is 512 pixels = 26" across.

(Program 7125: visits 4–6; root name = O42 V). The observations were so scheduled because, in September, the nominal roll of the telescope orients the disk midway between the telescope diffraction spikes. The observing

program consisted of three “visits,” each one orbit long and each at a different spacecraft roll angle. In each visit, the star was first located in the 6" target-acquisition “window” of the CCD. Then the telescope was moved to place the star

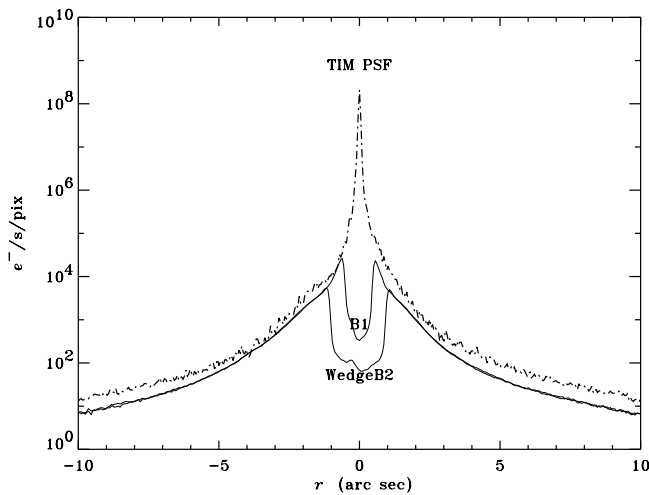


FIG. 5.—Performance of the STIS coronagraph as demonstrated by a comparison of computed (*dash-dotted line*) vs. observed PSFs. The apparent “noisiness” of the predicted profile stems from using only eight monochromatic PSFs to represent the PSF for the clear imaging mode. The observed radial flux profiles of the star are shown for WedgeB1 data (*solid line*) and WedgeB2 data (*heavy line*). Note the large rejection factor at the core of the PSF and the modest suppression of the halo.

behind the WedgeB2 occulting bar. Next, a series of eight 5 s exposures was recorded. Finally, the telescope was repositioned to place the star behind the WedgeB1 occulting bar and two sequences of eight 3 s exposures were taken.

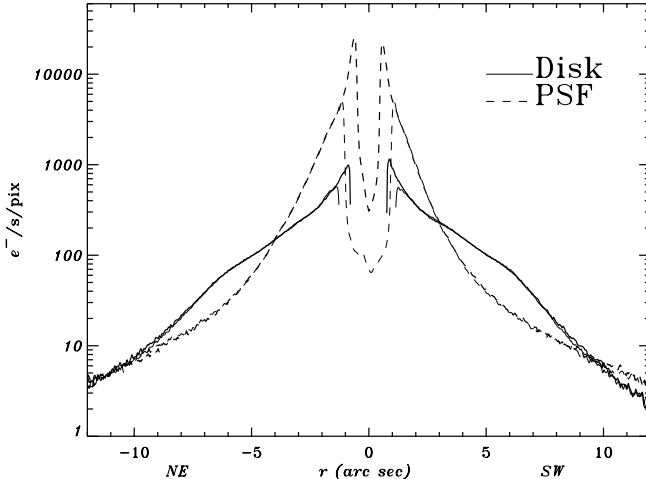


FIG. 6.—Radial flux profiles of the spine of the β Pic disk (*solid line*) and PSF (*dashed line*). The star is at the origin. Both WedgeB1 (*solid line*) and WedgeB2 (*heavy line*) profiles are shown.

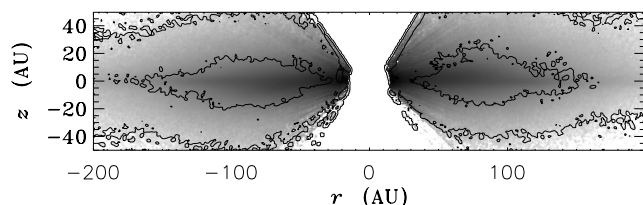


FIG. 7.—Data quality of the disk image. A gray-scale image shows the WedgeB1 observations of the disk on a logarithmic stretch. Contours of $S/N = 10$ and 100 per pixel are overlaid.

3.2. Data Reduction and Solution for the Disk

The data were reduced with the STIS Investigation Definition Team (IDT) version of CALSTIS.⁶ In this program, each series of eight exposures was collected into a data cube, where cosmic-ray hits could be identified and removed and a single average image formed. A bias image appropriate for a CCD gain of 4 was subtracted from the observed image. After conversion to count rates in $e^- s^{-1} \text{ pixel}^{-1}$, a dark image was subtracted. Hot pixels were identified and removed by reference to a hot-pixel table generated from dark frames made during the week of the observations. The resulting image was flat-fielded with a flat generated from imaging observations of a tungsten lamp. No sky subtraction was performed, since the sky background is very faint. The median pixel value far from the star is $0.4 e^- s^{-1} \text{ pixel}^{-1}$ on the WedgeB2 images and $0.2 e^- s^{-1} \text{ pixel}^{-1}$ on the WedgeB1 images. In any case, any residual sky light, assumed to be uniform over the field of view, is incorporated in the PSF and removed as part of the solution for the disk.

The diffraction spikes were used to determine the precise location of the star. Although the position of the star was stable during a given visit (telescope roll angle), the position of the star image on the CCD array changed by up to a pixel ($0''.05$) between visits. We therefore geometrically registered the images at the second and third roll angles with the first using the diffraction spikes as fiducials.

A software mask was applied to the diffraction spikes and the edges of the occulting bar in order that they not interfere with the solution for the brightness distribution of the disk. The effect of the software mask, however, is to limit imaging of the disk to distances $r > 0''.75 = 15 \text{ AU}$ (WedgeB1) and $r > 1''.24 = 24 \text{ AU}$ (WedgeB2) from the star. Also in preparation for separating the disk and stellar components of each image, a 512×512 pixel region centered on the star was extracted and expanded to 1024×1024 pixels.

Separation of the disk and star was achieved in an iterative process. As a starting approximation, the PSF was assumed to be the average of the images from each visit, each at a different orientation. The PSF was then subtracted from each image and the resulting residual images aligned by rotation and averaged to obtain a first estimate of the brightness distribution of the disk. The disk (rotated back to the observed orientation) was then subtracted from each image to get a new estimate of the PSF. This process was repeated 100 times. The solution also involved a rotation of the disk image by $0''.94$ in order to align the disk along a CCD column. Figure 4 shows the results for the WedgeB1 observations.

No reference star was observed, so it was not possible to make a complete check on the roll separation procedure. Instead, we used the image of HD 60753 (cf. Fig. 2), scaled to the brightness of β Pic, as a template PSF. Although this star is not a good match in spectral type to β Pic, it produces a residual image that is very similar to the disk images obtained by roll separation—except in the region close to the star, where the image of HD 60753 is saturated. Evidently, there is no confusion problem at distances of $1''.5$ or more from the star.

⁶ See CALSTIS Reference Guide by D. Lindler, at <http://hires.gsfc.nasa.gov/stis/docs/calstis/calstis.html>.

3.3. Evaluation of the Results

Since there are no experimental data available for evaluating the effectiveness of the occulting mask and Lyot stop, we compared the derived PSF for β Pic with theoretical models. Figure 5 compares the radial profile of the derived PSF with that computed from Telescope Imaging Modeling (TIM) models (Burrows & Hasan 1993). This plot demonstrates the two main advantages of coronagraphy. First, the $1''$ occulting wedge provides a rejection factor of up to 8000. Were it not for the wedge, the star would produce count rates of up to nearly a billion $e^- s^{-1} \text{ pixel}^{-1}$. But because the star is occulted, the dynamic range of the β Pic scene is lowered to a point where it can easily be accommodated by the CCD detector. For example, at $r = 0''.5$ (10 AU), the occulted star contributes $26,000 e^- s^{-1} \text{ pixel}^{-1}$, well below the full-well capacity of the CCD ($144,000 e^- \text{ pixel}^{-1}$) for a 1 s exposure. Since the readout noise of the summed image (eight or 16 exposures for WedgeB2 and WedgeB1, respectively) is below $1 e^- s^{-1} \text{ pixel}^{-1}$, its dynamic range is about 1×10^6 . Second, the wings of the PSF are a factor of 2 lower than the TIM model for the telescope performance. This level of suppression accords with the expected action of the Lyot stop, but further observations are needed to complete the characterization of the STIS coronagraphic mode.

Figure 6 compares the radial profiles of light from the star and from the midplane of the disk. The star contributes more light to the disk interior to $r = 3''$ and also beyond $9''$; this is because the sky background is included in the PSF. Figure 7 shows the disk image with contours of the associated signal-to-noise (S/N) ratios superposed. The errors used to compute the S/N for each pixel were estimated from

differences in the six different solutions for the disk (observations at three roll angles times two wedge positions). As such, they should represent a total error including both observational uncertainties and errors in the data processing. Along the spine of the disk, the signal-to-noise ratio exceeds 100 over the region from 30 to 150 AU from the star. Above and below the spine of the disk, the brightness, and consequently, the S/N, drop rapidly.

4. OBSERVED PROPERTIES OF THE β PIC DISK

4.1. Disk Morphology

Figure 8 shows the resulting images of the β Pic disk based on the WedgeB1 observations. At the top is a false-color image of the disk on a log scale. The bottom shows the disk with intensities normalized to midplane brightness and the vertical scale (i.e., perpendicular to the spine of the disk) expanded by a factor of 4 in order to show the shape of the disk more clearly. The main visual impressions are the smoothness of the disk and the presence of a warp close (in projection) to the star. The smoothness of the disk in the STIS images is in sharp contrast to previous images (Burrows et al. 1995; Mouillet et al. 1997), which are marked by swirls and radial spikes. We interpret this texture in previous images to incomplete elimination of the PSF. The pronounced warp in the disk was detected in previous images, but only the STIS images are able to follow it in close to the star. Below, we report on quantitative measurements of the disk, including the radial flux gradient and vertical flux distribution, the warp, and the innermost region of the disk ($r < 1''.5$), which heretofore has not been seen in images of its dust-scattered light. To describe the disk, we use a cylindrical coordinate system

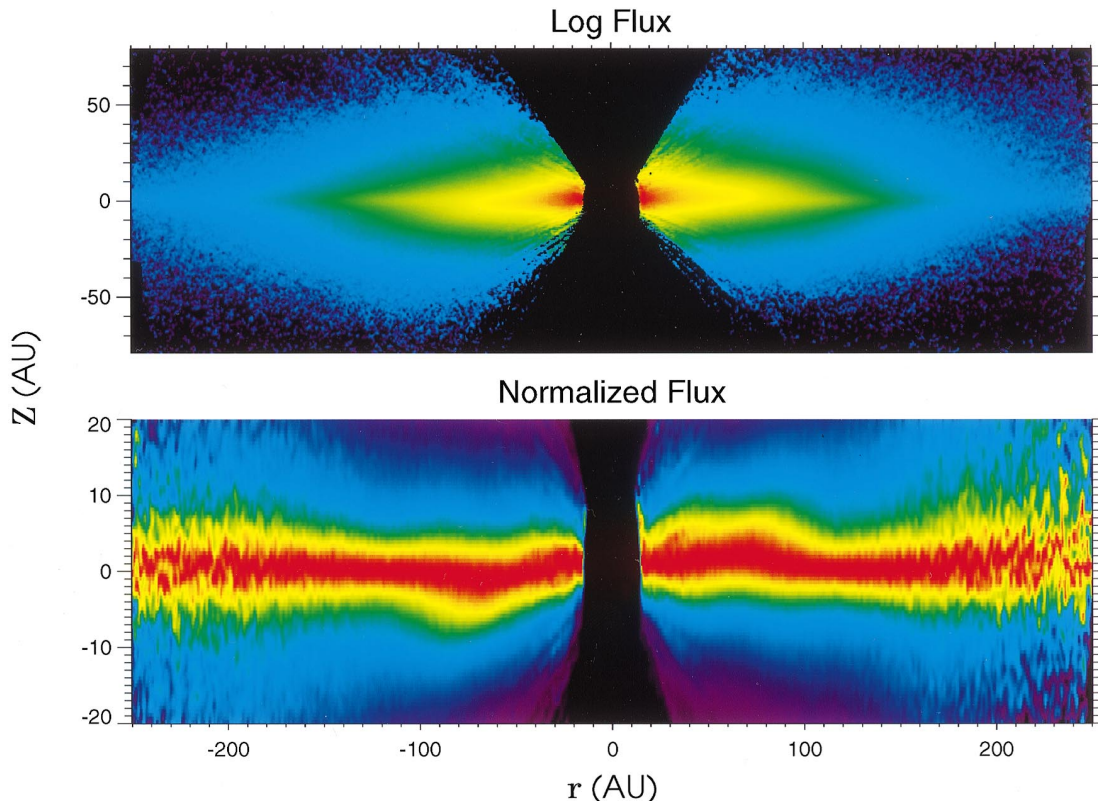


FIG. 8.—STIS/CCD coronagraphic images of the β Pic disk (WedgeB2 observations). The half-width of the occulted region is $0''.75 = 15$ AU. At top is the disk at a logarithmic stretch. At bottom is the disk normalized to the maximum flux, with the vertical scale expanded by 4.

with r denoting the projected distance from the star along the disk midplane and z being the distance perpendicular to the disk plane (“vertical” distance).

We measured the radial profile of the disk in three different ways: (1) along the midplane defined by the outer disk, averaging over a swath ± 1.25 AU high; (2) along the curved spine (position of maximum flux), again averaging over a swath ± 1.25 AU high; and (3) along the midplane, but totaling the flux within a swath ± 100 AU high. Figure 9 shows the radial brightness profile of the disk along its midplane (method 1). It shows that the brightness distribution has three segments: an inner region with a rather flat brightness distribution, a transition region, and an outer region where the flux falls off rapidly with increasing radius. We fit the inner ($r = 1''.6-3''.7$) and outer ($r = 6''.7-9''.0$) segments of the profile by a power law, $I(r) = r^\gamma$. Table 1 lists the resulting values of γ for all three methods of measurement.

Table 2 compares our results with previous measurements. In qualitative agreement with others, we find the

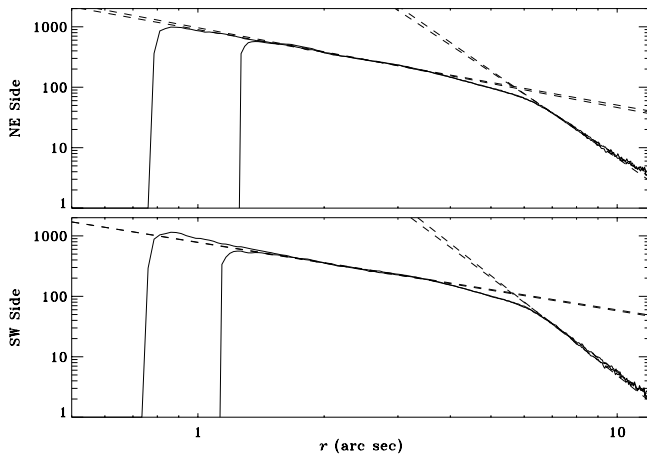


FIG. 9.—Midplane surface brightness of the β Pic disk (counts s^{-1} pixel $^{-1}$) as obtained from WedgeB1 observations (solid line) and WedgeB2 observations (heavy line). The northeast extension is on top, the southwest extension at bottom. The dashed lines show power-law fits to the brightness distribution of the inner region ($1''.65 < r < 3''.67$) and outer region ($6''.7 < r < 9''.0$). The power-law indices are listed in Tables 1 and 2.

TABLE 1
RADIAL INDEX MEASUREMENTS

MEASUREMENT	NORTHEAST SIDE		SOUTHWEST SIDE	
	Outer	Inner	Inner	Outer
Spine (1)				
WedgeB1	-4.59	-1.25	-1.13	-5.18
WedgeB2	-4.81	-1.32	-1.12	-5.49
Maximum (2)				
WedgeB1	-4.57	-1.24	-1.05	-5.17
WedgeB2	-4.76	-1.30	-1.02	-5.44
Total (3)				
WedgeB1	-3.83	-0.89	-0.96	-4.08
WedgeB2	-4.46	-0.95	-0.87	-5.17

NOTE.—Labels 1, 2, and 3 refer to methods of measurement described in the text.

TABLE 2

COMPARISON WITH PREVIOUS MEASUREMENTS

Region (Radius)	Northeast	Southwest	Reference
1''.6-3''.7	-1.28 ± 0.04	-1.12 ± 0.01	1
2''.8-6''.0	-1.79 ± 0.01	-1.74 ± 0.04	1
3''.0-6''.0	-1.3	-1.3	2
2''.8-6''.0	-2.40 ± 0.24	-2.47 ± 0.36	3
2''.4-5''.5	-2.38 ± 0.72	-1.91 ± 0.89	4
6''.7-9''.0	-4.80 ± 0.1	-5.50 ± 0.1	1
> 6''	-3.5	-3.5	2
6''.0-16''.0	-3.76 ± 0.05	-4.07 ± 0.05	3
6''.0-16''.0	-3.508 ± 0.0003	-4.182 ± 0.0004	4

REFERENCES.—(1) This paper. (2) Mouillet et al. 1997. (3) Kalas & Jewitt 1995. (4) Golimowski, Durrance, & Clampin 1993.

following: the northeast and southwest sides of the disk are similar at equal radii for $r < 6''$; there is a major change in the brightness gradient at $r \approx 6'' = 120$ AU; beyond $r = 120$ AU, the northeast and southwest sides of the disk differ appreciably in brightness and shape. In other respects, the STIS results are quite different from those of previous studies. In the STIS images, the brightness profile of the inner disk is significantly flatter—more in accord with thermal IR images (Pantin, Lagage, & Artymowicz 1997)—and the outer disk much steeper. Thus, the change in slope at $r \approx 6''$ is much more dramatic in the STIS images ($\Delta\gamma \approx 4$). Evidently, there is a very real change in the density distribution of dust and/or in the scattering properties of the dust at 120 AU from the star.

Figure 10 shows a contour plot of the disk at brightness levels equal to 0.1, 0.5, and 0.99 times the maximum brightness at a given projected radius. The STIS coronagraphic images probe the disk in scattered light closer to the star than previous observations. It is striking that the disk is seen right up to the WedgeB1 (software) mask edge at a projected distance of 15 AU from the star. The WedgeB1 (solid line) and WedgeB2 (heavy line) observations agree quite well except at very low surface brightness, where the disk in the WedgeB1 image is more distended vertically

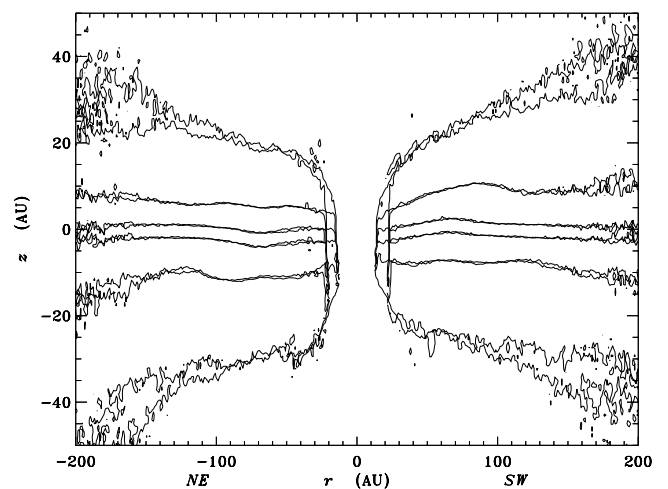


FIG. 10.—Contour plot of the β Pic disk for both the WedgeB1 observations (solid line) and WedgeB2 observations (heavy line). Three brightness levels are shown: the spine of the disk ($\geq 99\%$ of the maximum brightness), the full width at half-maximum brightness, and contours at 10% of the maximum brightness.

than in the WedgeB2 image. We interpret this discrepancy as an indication of uncertainties in the data at low brightness levels. The spine of the disk (99% contours) has an approximately constant thickness but is curved. At half-maximum brightness, the disk shows bulges on either side (Table 3) that are almost round and pinched off smoothly at either end. The full width at 0.1 maximum (FW0.1M) increases with distance from the star, consistent with a constant opening angle (wedge shape).

The curvature of the spine of the disk is shown in more detail in Figure 11, which shows both WedgeB1 (solid line) and WedgeB2 (heavy line) observations. The two observations give consistent results. The tilt of the inner disk is seen clearly. However, the extensions of the two sides of the inner disk do not meet at the star. Instead, the spine of the disk dips below the disk equator close to the star ($r < 1''.5 = 30$ AU). Like Kalas & Jewitt (1995), we interpret this “wing tilt” asymmetry as the consequence of forward-scattering particles in a disk that is inclined to the line of sight. Because of forward scattering, the side of the disk that is closer to the observer will be brighter than the far side. In the case of β Pic, the closer side of the disk is evidently the lower (southeast) side. Midway out from the star ($r = 30$ – 120 AU), the spine is curved. It has its greatest amplitude, $\Delta z \approx \pm 1.5$ AU, at $r \approx 70$ AU, somewhat closer in than the bulges revealed by the FWHM contours in Figure 10.

4.2. Component Structure of the Disk

Figure 12 shows the vertical brightness profile at $r = 90$ AU, where the bulges are most pronounced. The asymmetrical profile suggests the presence of two components: a

TABLE 3
THICKNESS OF DISK (IN AU)

R (AU)	FWHM	FW0.1M
20	17	34
50	16	45
100	18	54
120	15	55
200	22	66

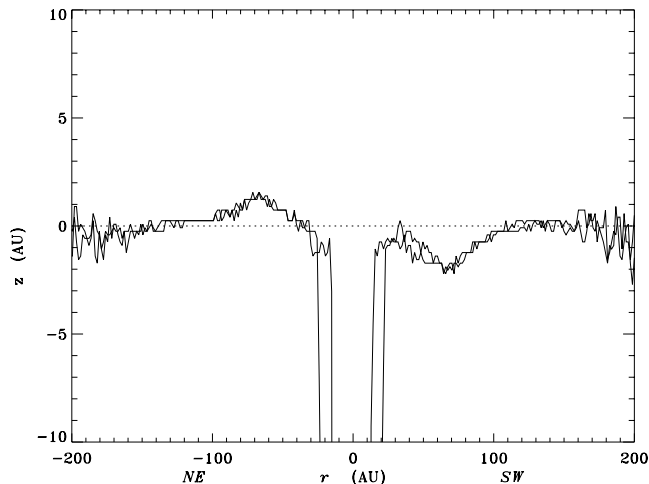


FIG. 11.—Curvature of the spine of the β Pic disk as indicated by the WedgeB1 observations (solid line) and WedgeB2 observations (heavy line).

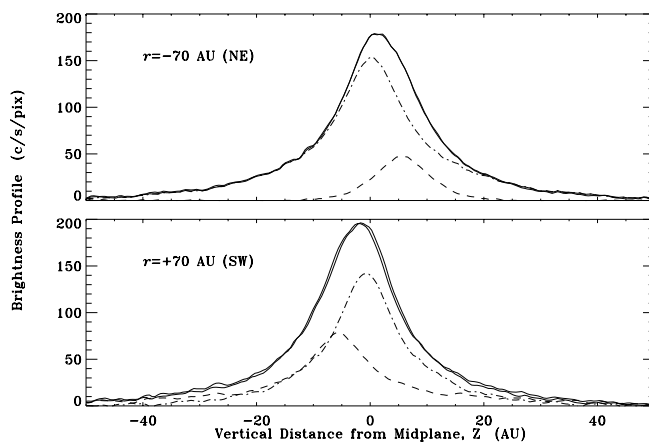


FIG. 12.—Vertical brightness profiles of the disk at $r = 90$ AU on the northeast side (top) and southwest side (bottom). The observed profile is shown in bold, the two components as dashed lines, and the sum of the two components as the solid line.

main component that defines the orientation of the disk and a fainter component that is offset from the main component. By assuming that each component is symmetric vertically, we were able to separate the two components. The results of the decomposition (Fig. 13) indicate that the fainter component is inclined by 4.6° with respect to the main component. The decomposition breaks down close to the star ($r < 50$ AU) partly because the offset of the inclined component becomes much smaller (< 4 CCD pixels) than the thickness of the disk. Also, errors in the disk structure induced by roll separation of the disk (§ 3.1) are likely to be significant close to the star. Far from the star, the solution is noisy because of the faintness of the disk.

Figure 14 shows the radial flux distributions of the total disk (both main and tilted components) and tilted components. While the inclined component is detectable at large distances from the star, its brightness beyond ≈ 80 AU falls off so rapidly that it is not noticeable in the STIS images, and the measurements are suspect. Inward of 80 AU, its brightness declines, suggesting a central cavity, especially on the northeast side. At all projected distances from the star, the southwest side of the tilted component is the stronger, whereas the southwest side of the main component (not shown) is somewhat weaker.

The tilted component detected by STIS shows a strong similarity to the inner part of the disk viewed in the thermal IR at $12 \mu\text{m}$ by Pantin et al. (1997). First, its position angle

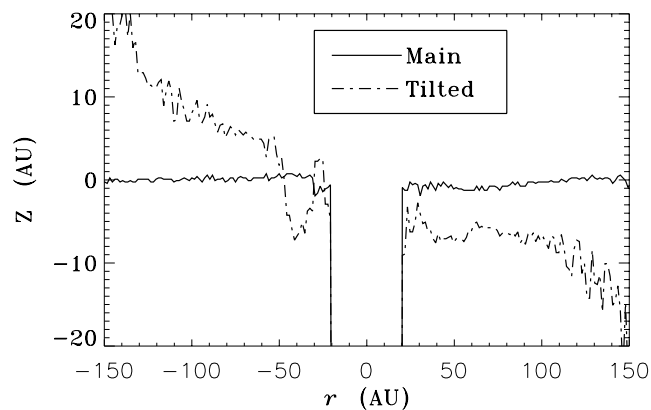


FIG. 13.—Vertical offsets of the two components

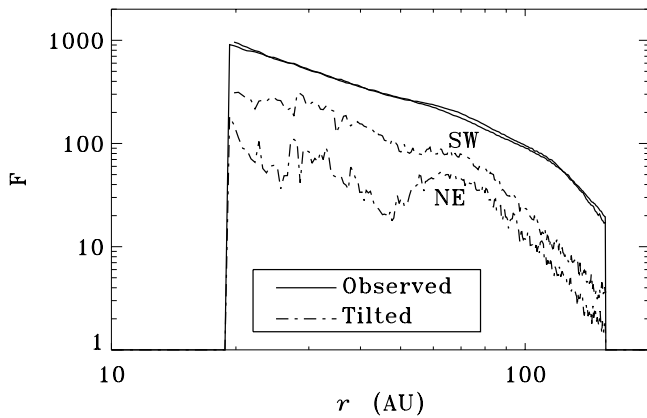


FIG. 14.—Radial brightness profile of the observed (solid line) and tilted (dash-dotted line) components.

is $P.A._{\text{tilt}} = 35^{\circ}.4 = 4^{\circ}.6 + 30^{\circ}.8$ (we use the average position angle measured by Kalas & Jewitt 1995 for the position angle of the main component), the same as the measured position angle of the IR disk, $P.A._{\text{IR}} = 35^{\circ}.4 \pm 0^{\circ}.6$ (E. Pantin 1998, private communication). Second, the southwest side of the tilted component is brighter than the northeast side, as is the case for the IR disk, where the southwest side is nearly 3 times brighter at $r \approx 3''.6$. Finally, the tilted component shows evidence of a downturn in brightness at $r < 2''.5$, suggestive of a central cavity. Taken by itself, this evidence would be viewed with skepticism in view of potential errors produced in roll separation (§ 3.1). However, it is consistent with the IR data, which are not vulnerable to such errors.

The overall multiwavelength structure of the disk becomes clearer and more intriguing with the recent submillimeter maps of the β Pictoris system reported by Holland et al. (1998). At $850 \mu\text{m}$, the disk out to $r \approx 15''$ is an elongated structure whose position angle ($P.A. = 32^{\circ} \pm 4^{\circ}$) is consistent with the orientation of the main component of the optical disk. However, there is an emission patch farther out from the star ($r = 33''$) whose position angle, $P.A. = 37^{\circ} \pm 6^{\circ}$, is more in line with the tilted component seen by STIS.

Based on these comparisons with IR and submillimeter images, we identify the tilted component as the inner part of the disk seen in the infrared. We suggest that past interactions in and ejection from the inner disk are responsible for the submillimeter blob much farther out. We tentatively identify the main disk component as material primarily farther out from the star than ≈ 80 AU.

5. INTERPRETING THE WARP IN THE DISK

There are two theories about the origin of the warping of the β Pic disk. In one, the observed warp is formed by the gravitational attraction of a planet in an orbit inclined to the dust disk (Burrows et al. 1995). A similar conclusion was reached by Mouillet et al. (1997), who made numerical simulations to show how the gravitational pull of a major planet in orbit 3–20 AU from the star could warp the disk further out where the bulges are seen. In the other theory, developed by Armitage & Pringle (1997), warps naturally form in the inner part of accretion disks surrounding luminous ($\geq 10 L_{\odot}$) pre-main sequence stars because of a radiation-induced instability. Both theories predict that the disk will look the same for many thousands of years. The

two theories differ, however, in the predicted size and shape of the warp and in their assumptions about the star. With their high image quality and high resolution, the STIS images present stringent observational tests of the models. Below, we compare the STIS observations with predictions of the two theories.

5.1. Radiation-Induced Warps

Armitage & Pringle's simulations (Armitage & Pringle 1997) follow the development of a radiatively induced warp in $L \geq 10 L_{\odot}$ stars over the lifetime of the warp (about 20 Myr). In its initial stages, the warp looks like a spiral wave coming out from the star, with its greatest amplitude close to the star (see Fig. 3 of Maloney, Begelman, & Pringle 1996). The amplitude of the warp grows to several tens of degrees in a few Myr but then decays on a viscous timescale (a few Myr) when the disk becomes optically thin. Over the course of time, the spiral wave washes out so that the disk looks more symmetrical. According to this theory, the β Pic disk is well into the decay stage.

The inner region of the model disk, while flat and quite thin during the decay phase, is tilted with respect to the outer regions of the disk, but the tilted region extends out only to about 25 AU from the star. If the line of nodes is aligned with the line of sight, the maximum thickness of the disk would occur at $r = 1''.2$. Regardless of the angle of the line of nodes, the apparent thickness should decrease at $r > 1''.2$. This is not the case: the observed disk has its maximum vertical thickness in the bulge region at $r = 4''.5 = 90$ AU.

Another problem for the theory concerns the properties of the star. In order for a radiation-induced warping mechanism to be viable, β Pic must be less than about 20 Myr old, and its luminosity must exceed $10 L_{\odot}$. In interpreting the disk of β Pic, Armitage & Pringle (1997) assumed the stellar parameters derived by Lanz, Heap, & Hubeny (1995). However, these parameters have been revised because of the new, accurate distance to β Pic from *Hipparcos* (Crifo et al. 1997) and new, accurate spectrophotometry of β Pic from 3200 to 7350 Å (Alekseeva et al. 1996). The new data imply a somewhat lower stellar temperature than before, $T_{\text{eff}} = 7950$ K, a lower luminosity, $L = 8 L_{\odot}$, and a minimum age of about 20 Myr.

We conclude that radiation-induced warping is ruled out by observation: the observed warping extends out 3 times farther than predicted; at $L = 8 L_{\odot}$, the star does not have the luminosity needed to induce warping; and at ≥ 20 Myr, the system is too old for warping to be detectable.

5.2. Warping by a Planet

In the planetary-perturbation theory (Larwood & Pappalouizou 1997 and references therein) the shape of the warp depends on the orbital parameters of the planet. For example, if the planet is in an elliptical orbit, one side of the tilted inner disk would extend out farther from the star than the other. The radial extent of the warp scales with $(M_P a^2 t)^{2/7}$, where M_P is the mass of the perturber, a , the semimajor axis, and t , the age of the system. The STIS observations showing that the disk is warped out to 70 AU or more (Mouillet et al. 1997 used 50 AU) require that

$$\log(M_P/M_{\star}) + 2 \log a + \log t \approx 6.7,$$

where a is in AU and t is in yr. Furthermore, we require that $M_P/M_{\star} \leq 0.01$; otherwise, the perturber would induce

TABLE 4
POSSIBLE MASS OF PERTURBING
OBJECT (IN M_J)

a (AU)	AGE (Myr)		
	20	50	100
3	48	19.4	9.7
5	17.4	7.0	3.5
10	4.4	1.7	0.87
15	1.9	0.77	0.39
20	1.09	0.44	0.22
30	0.48	0.19	0.10
50	0.17	0.07	0.035

stellar radial velocity variations that are not observed ($\Delta RV < 1 \text{ km s}^{-1}$ according to A.-M. Lagrange 1998, private communication). Table 4 gives some possible values of the mass of the perturber implied by this equation for orbital sizes ranging from 3 to 50 AU and for ages ranging from 20 to 100 Myr. It shows that if the β Pic system is young ($t \approx 20$ Myr) and the companion is very close to the star ($a < 3$ AU), the warp is produced by a brown dwarf or a very low mass star. If the perturber is farther away (5–50 AU), then the corresponding planetary mass ranges from 17.4 to 0.17 M_J , where M_J is the mass of Jupiter. If the system is more evolved ($t \approx 100$ Myr), the same orbital parameters imply a lower planetary mass, down to 10 times the mass of the Earth.

6. CONCLUSIONS AND FUTURE WORK

Coronagraphic performance of STIS.—Observations of β Pic indicate that the STIS coronagraphic aperture and Lyot stop are effective in blocking light from the star. The rejection factor at the PSF core is as high as 8000 even for occulting masks as small as $1''.0$ in width ($1''.5$ after the software mask is applied). There is also some suppression of the PSF halo, but further observations will be needed to quantify this performance feature. The PSF has significant structure but is generally stable on a timescale of minutes and days. Because of this stability, the PSF can be substantially removed from the data.

Observed properties of the β Pic disk.—The STIS images clearly define the warp with high precision and at close radii

to β Pic. They show that the observed warping of the disk can be resolved into two disks 5° apart. We interpret the brighter component as arising primarily in the outer disk and the fainter component as arising in the inner region of the disk.

Presence of planet(s) in the β Pic disk?—The observed properties of the tilted inner disk are consistent with the presence of a planet in the disk. Table 4 gives possible masses and orbital sizes of the planet. The STIS observations are consistent with the planetary hypothesis, but before definitive testing of planet-warped models can proceed, they first need to be combined with thermal-emission images in the IR and submillimeter in order to identify the major dynamical processes operating in the disk and to refine the possible parameters of the perturber. One issue to be resolved by the combined observations is the size of the central clearing zone, since that gives an upper limit to the semimajor axis of a planet's orbit. Another issue is the orbital eccentricity of the perturbing object. An eccentric planetary orbit ($e > 0.1$) has been invoked to explain spectral absorption features formed by “falling evaporating bodies.” The thermal IR images are ideal in characterizing asymmetries in the inner disk, which could then be used to constrain the eccentricity. We believe that the STIS images described here, when combined with IR and submillimeter images, should prove useful in constructing a comprehensive model of the disk.

The observations presented here represent a first exploration of the β Pic disk with STIS. Future observations should bring substantial improvement. For example, we can check the present results by observing a suitable reference star and subtracting the image from the β Pic observations to isolate the disk. We plan to follow up the present observations with additional measurements, including coronagraphic spectroscopy.

We thank Merle Reinhart, the program coordinator for program 7125, for accomplishing the challenging scheduling of the β Pic observations. We also thank Chris Burrows, Hashima Hasan, and Mark Clampin for their work in computing the telescope point-spread function. We gratefully acknowledge the advice of Pawel Artymowicz, who suggested that we try decomposing the disk. We also acknowledge the helpful criticisms and suggestions of the anonymous referee. This study was supported by NASA via a grant to the STIS IDT.

REFERENCES

- Alekseeva, G. A., et al. 1996, *Baltic Astron.*, 5, 603
 Armitage, P. J., & Pringle, J. E. 1997, *ApJ*, 488, L47
 Artymowicz, P. 1997, *Annu. Rev. Earth Planet. Sci.*, 25, 175
 Burrows, C., & Hasan, H. 1993, *The Telescope Imaging Modelling Users Manual* (Baltimore: STScI)
 Burrows, C., Krist, J. E., Stapelfeldt, K. R., & WFPC2 Investigation Team. 1995, *BAAS*, 187, 3205B
 Crifo, F., Vidal-Madjar, A., Lallement, R., Ferlet, R., & Gerbald, M. 1997, *A&A*, 320, L29
 Golimowski, D. A., Durrance, S. T., & Clampin, M. 1993, *ApJ*, 411, L41
 Holland, W. S., et al. 1998, *Nature*, 392, 788
 Kalas, P., & Jewitt, D. 1995, *AJ*, 110, 794
 Kimble, R., et al. 1998, *ApJ*, 492, L83
 Lanz, T., Heap, S. R., & Hubeny, I. 1995, *ApJ*, 447, L41
 Larwood, J. D., & Papaloizou, J. C. B. 1997, *MNRAS*, 285, L288
 Maloney, P. R., Begelman, M. C., & Pringle, J. E. 1996, *ApJ*, 442, 582
 Mouillet, D., Larwood, J. D., Papaloizou, J. C. B., & Lagrange, A. M. 1997, *MNRAS*, 292, 896
 Pantin, E., Lagage, P. O., & Artymowicz, P. 1997, *A&A*, 327, 1123
 Sahu, K., et al. 1999, *STIS Instrument Handbook* (Baltimore: STScI)
 Smith, B. A., & Terrile, R. J. 1984, *Science*, 226, 1421
 Vaughn, A. 1991, *HIORP report* (Pasadena: Jet Propulsion Laboratory)
 Vidal-Madjar, A., et al. 1994, *A&A*, 290, 245
 Woodgate, B., et al. 1998, *PASP*, 110, 1183